RESEARCH

Impact of cavitation and inflow perturbation on the performance of a horizontal-axis tidal turbine

Alessandro Capone[1] · Fabio Di Felice[1] · Francesco Salvatore[1] · Harish Maddukkari[1] · Nicholas Kaufmann[2] · Ralf Starzmann[2]

Abstract

The impact of cavitation and inflow perturbation by an upstream support structure on the performance of a horizontal-axis tidal turbine has been studied by experiments at model scale in a depressurized water channel at CNR-INM. Measurements of turbine generated power and thrust have been carried out at varying channel flow speed, tip-speed ratio, and cavitation number. The visualization of cavitation patterns has been associated with the performance measurements to identify the role played by different cavitation types on turbine behavior. Radiated noise measurement were also performed to assess the impact of cavitation phenomena on turbine induced acoustic signature.

Keywords Tidal energy · Horizontal-axis turbine · Tidal current turbine · Cavitation

1 Introduction

The increase of energy production from renewable resources is at the heart of the transition from an economy based on fossil fuel to one relying upon low carbon emissions. The current trend is to reduce the dependence on fossil fuels by significantly increasing the energy production from wind and solar sources. In spite of the competitive cost of these energy sources, a major drawback is represented by the limited predictability of the resource with problems in balancing energy production and demand in the grid. In this context, an important contribution to improve the reliability of the renewable

energy mix can be given by the exploitation of marine tidal currents. The driving mechanism associated with the mutual gravitational attraction in the Earth/Moon/Sun system yields that the tidal energy resource is predictable with extreme precision in the long term which is a distinctive advantage over other resources. The feasibility of tidal energy exploitation has been widely investigated over the last 2 decades (see among others Bahaj and Myers 2004). The technology is still at early stage of development and several projects are underway to de-risk the installation of market-ready devices. At present, the majority of developers are working on instream horizontal-axis turbines for both seabed-fixed and floating installations (Kempener and Neumann 2014).

It is well known that the vast corpus of knowledge and research existing on wind turbines has been extended to marine tidal turbines design (see, e.g., the seminal work by Hansen and Butterfield (1993)). By leveraging on this common basis, research in the tidal sector is focused on developing specific knowledge on physical mechanisms having a direct impact on the reliability, efficiency, and sustainability of energy-harvesting systems operating in the harsh marine environment. Turbine blades are designed to face hydrodynamic loads characterized by significant intensity fluctuations due to the non-uniformity of the onset flow. Tidal stream turbulence as well as interaction with surface waves are among the main sources of fatigue loads. Experimental works by Mycek et al. (2014a, b) investigate the role of

✉ Alessandro Capone
  alessandro.capone@cnr.it

  Fabio Di Felice
  fabio.difelice@cnr.it

  Francesco Salvatore
  francesco.salvatore@cnr.it

  Nicholas Kaufmann
  nkaufmann@schottel.de

  Ralf Starzmann
  rstarzmann@schottel.de

[1] CNR Institute of Marine Engineering, Via di Vallerano 139, Rome 00128, Italy

[2] SCHOTTEL Hydro, Mainzer Strasse 99, Spay 56322, Germany

incoming turbulence intensity on a single turbine and in the case of two aligned devices. More recently, (Lee et al. 2020) describe the results of turbine wake flow measurements (up to 7 and 20 rotor diameters, respectively) by Acoustic Doppler Velocimetry in a large depressurized water channel and in an open channel flume, respectively. The role of turbine immersion is analyzed by Bahaj et al. (2007) by towing tank experiments, whereas the interactions among wakes downstream of turbine arrays are analyzed in Gajardo et al. (2019) by numerical simulations.

Cavitation, which occurs when the static pressure falls below the water vapor pressure, has been extensively studied for marine propulsors and hydraulic machinery (Aktas et al. 2016, Aktas et al. 2016 among others). Main detrimental phenomena associated with the collapse of cavities include noise emissions, structural vibrations, erosion, and loss of efficiency. The impact of radiated underwater noise on marine ecological systems and, to a wider extent, on economical systems has been studied and assessed by several authors (refer to Hildebrand (2009) and Frisk (2012) among others). Cavitating–flow phenomena are potentially harmful for hydrokinetic turbines that operate close to the free surface, as in the case of floating systems. Increased levels of structural vibrations associated with cavitation may represent a critical issue for blades in composite materials, with significant reduction of system reliability if not properly addressed. Furthermore, as cavitation can lead to efficiency losses, a full comprehension of the operation of turbines under such conditions is pivotal for the design process and the optimization of the operational range. Despite the importance of cavitation for tidal turbines, existing studies on the subject are limited. Early works by Bahaj et al. (2007) and Wang et al. (2007) show how tidal turbine blades may undergo massive vaporized-flow regions on the blade surface, cavitating bubbles, as well as tip–vortex cavitation at relatively shallow depth. In their work, (Shi et al. 2016) present the results of radiated noise measurements and cavitation observations for a turbine featuring a bio-mimetic blade trailing edge. In a recent work, Rosli et al. (2020) presents cavitation and noise measurement tests for an unconventional design turbine and report the presence of tip–vortex cavitation in the operational range of the turbine. Cavitation inception predictions by computational modeling have been presented by Kaufmann et al. (2017) and Wimshurst et al. (2018). In the latter, the authors focused on the role played by blockage effects on cavitation inception and concluded that a safety margin in cavitation analyses should be considered to account for the pressure fluctuations caused by free-surface waves. In Sun et al. (2022), the authors propose a methodology for tidal turbine blade design based on simulations and a cavitation model to obtain a cavitation-free design.

Despite some recent works on the subject, there is still a lack of experimental data on turbine performance in cavitating-flow conditions. Another important aspect is represented by the fact that usually model scale testing as well as numerical modeling of tidal turbines are based on ideal flow conditions, in which the rotor is subjected to uniform axial flow. As a matter of fact, the presence of obstacles perturbing the incoming flow to the rotor disc may have a remarkable impact, with the induction of transient cavitation phenomena that are typically associated with higher levels of radiated noise and erosion risks. To the authors' knowledge, there is a literature gap on this subject.

The present work aims to give a contribution to the characterization of the impact of cavitation on the performance of a horizontal–axis tidal turbine. The study is carried out by testing a small-scale model turbine in the depressurized circulating water tunnel of the Institute of Marine Engineering of the Italian National Research Council (CNR-INM). Turbine operation in both ideal, uniform flow conditions, and in the perturbed onset flow generated by a supporting structure to deploy the turbine from a floating barge are considered. The turbine and supporting structure assembly reproduces the installation of Schottel Hydro SIT 250 turbines on the PLAT-I floating tidal energy system jointly developed with the Sustainable Marine Energy company (Starzmann, 2021; Jeffcoate, 2021; Jeffcoate et al. 2015). The experimental study combines turbine performance measurements, cavitation pattern visualizations, and radiated noise recordings to provide a comprehensive dataset that is expected to de-risk the design of tidal turbines by mitigating the effects of cavitation.

The manuscript is organized as follows. The experimental setup, the testing facility, and the test matrix are described in Sect. 2. The results of the experimental study are presented and discussed in Sect. 3. This includes the analysis of cavitating-flow phenomena under variable turbine loading and inflow speed conditions. Cavitation inception conditions are determined and the impact of fully developed cavitation on turbine thrust and power is discussed. Acoustic noise emissions in both non-cavitating and cavitating-flow conditions are compared. Finally, the effect of the supporting structure perturbing the inflow to the turbine is presented and discussed.

2 Experimental setup

2.1 Turbine model

The model turbine is a three-bladed, 500 mm in diameter D, 1:8.6 scaled version of the SCHOTTEL Instream Tidal (SIT) horizontal-axis turbines which are currently installed on Sustainable Marine Energy's platforms PLAT-I 4.63 and PLAT-I 6.40 (Fig. 1). The latter is a 420 kW floating tidal energy platform developed in 2021 and deployed in the Bay of Fundy,

Fig. 1 Schottel hydro-SIT turbines installed on the Sustainable Marine Energy platform PLAT-I 6.40

Table 1 Turbine model data

Blades	3, Fixed pitch
Rotation	Clockwise, (as seen from upstream)
Diameter	500 mm
Model scale	1:8.6
Pitch angle, 70% span	7°
Blade chord, 70% span	40 mm
Hub/rotor diameter ratio	0.1
Blade section profile	SCHOTTEL Hydro design

Nova Scotia, Canada, which will form part of the world's first floating tidal energy array. The device is currently undergoing commissioning and testing in Grand Passage before it is deployed to Fundy Ocean Research Centre for Energy (FORCE). The turbines operate downstream of a movable strut as part of the SIT Deployment Module (SDM); Fig. 1. Details on turbine model geometry are provided in Table 1.

2.2 Facility and instrumentation setup

The experimental study was performed in the CNR-INM depressurized circulating water channel, a free-surface cavi-

tation flume tank with a test section of 3.6 m in width, 2.25 m in depth from the free surface, and 12.4 m in length; see Fig. 2. The maximum velocity that can be achieved in the test section is 5.2 m.s^{-1} and the pressure can be reduced to a minimum of 30 mbar to establish cavitating-flow similitude with full-scale conditions. The freestream turbulence in the test section is 2.5% of the mean inflow velocity and the velocity flow uniformity is within 1% across the section. Following (Day et al. 2015), turbine performance and cavitation tests were performed according to the ITTC recommended procedures 7.5-02-07−03.9 (hydrokinetic turbines, ITTC-Propulsion-Committee (2021a)) and 7.5-02-03−03.5 (cavitation, ITTC-Propulsion-Committee (2017)). The turbine was equipped with a 15kW brushless motor with a dedicated control unit for the imposed rotational speed. The setup includes a Kempf & Remmers dynamometer to measure turbine torque (Q) and thrust (T). Dynamometer data are acquired by a dedicated PC unit, with an acquisition frequency of 50000 Hz for 25 s for each tested condition. The resulting accuracy of the average torque and thrust measurements is 1% with a confidence interval of 95%, based on a t-Student distribution.

Radiated noise measurements were carried out by means of a hydrophone located in the upper side of the test section, lying within the rotor plane and at a distance D from the rotor axis. Two PCO Pixelfly camera with resolution 1392 X 1040 pixels fitted with a 80 mm lens were used to observe cavitation patterns on turbine blades. One camera was placed at turbine side and perpendicular to its axis, whereas the other one was placed slightly behind the turbine with approximately 35° angle facing toward the suction side of the rotor blades. Camera acquisitions were synchronized to a strobe lamp, so that pictures were acquired with the rotor blade in the same angular position. During cavitation tests, observations of the cavitation patterns were performed via the mentioned cameras, while simultaneously turbine performance and underwater radiated noise were recorded.

Fig. 2 Schematic view of the CNR-INM depressurized water channel
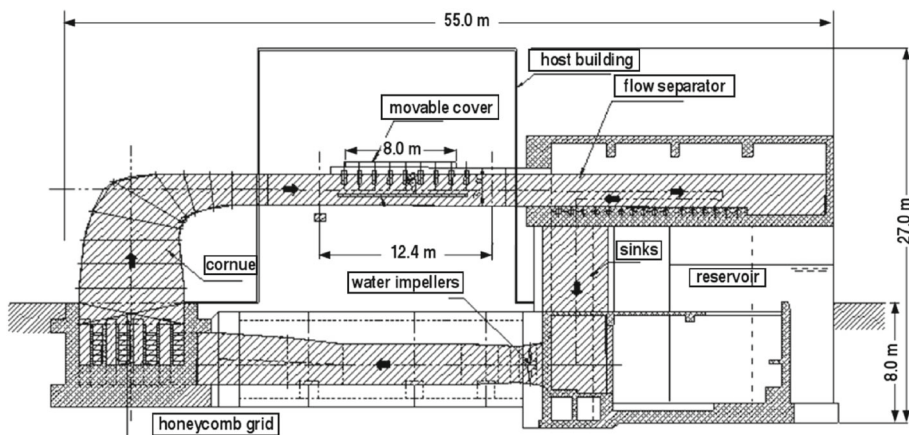
2.3 Test matrix

Turbine performance and cavitation tests were carried out in two configurations: *(i)* isolated turbine without SDM support structure (no–strut condition), and *(ii)* real-world condition with the SDM support structure mounted upstream of the turbine (behind–strut condition). For the purpose of testing, a simplified version of the SDM support structure with an inclined strut and a cylindrical nacelle was designed. The structure is separated by the turbine boss by a 5 mm gap and is fixed to a top frame piercing the free surface. Model SDM nacelle and strut were realized by 3D-printing, with a reinforcing aluminum bar inside the strut, whereas the turbine rotor was CNC-milled from

stainless steel. Schematics of the experimental setup are given in Fig. 3 for both no-strut and behind-strut configurations. Pictures of the same setup in the facility test section are shown in Fig. 4.

For both no-strut and behind-strut conditions, five inflow velocities U_∞ were considered, from $1.5\,\mathrm{m.s^{-1}}$ to $3.25\,\mathrm{m.s^{-1}}$. For each U_∞ case, 16 values of turbine rotational speed ω were tested to sweep a full range of variation of operating conditions from stall to freewheeling. Specifically, the Tip-Speed Ratio $\lambda = \omega R/U_\infty$, where $R = D/2$ is the turbine radius, was varied between 0.67 and 10.

The turbine performance is characterized in terms of thrust coefficient C_T, torque coefficient C_Q, and power

Fig. 3 Schematics of experimental setup for turbine tests, no-strut configuration (left) and behind-strut configuration (right). Strut dimensions (bottom)
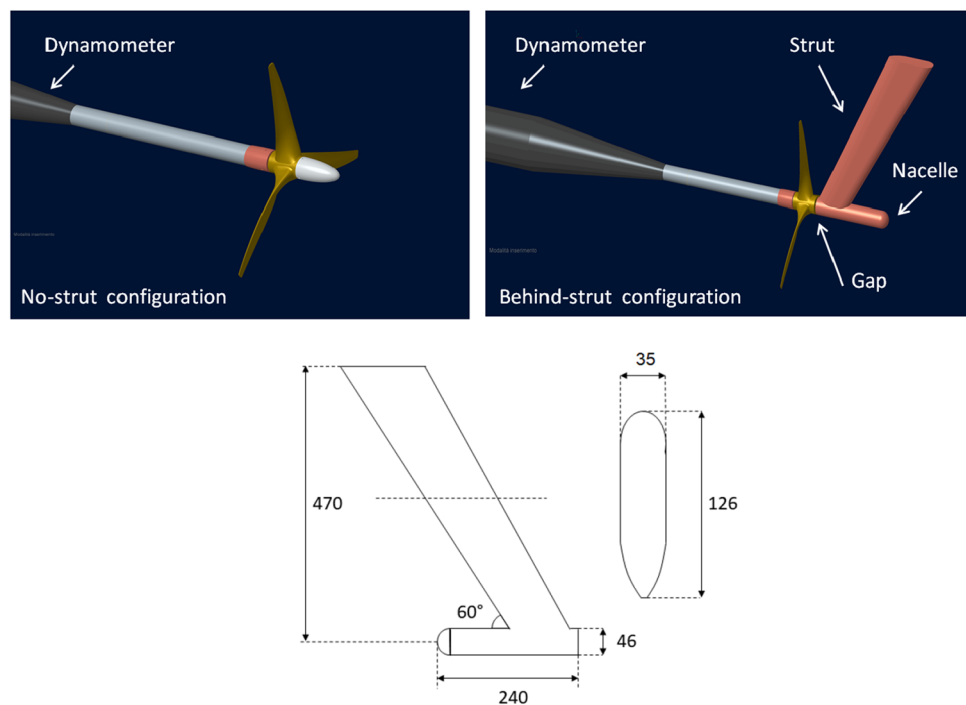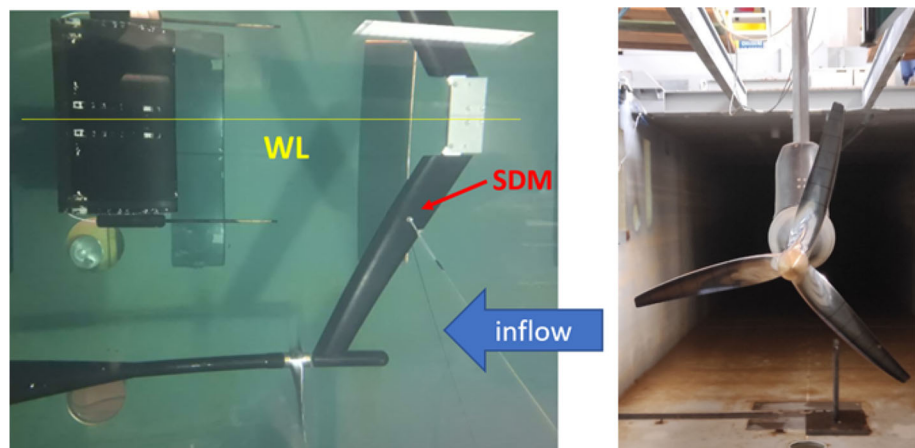

Fig. 4 Cavitation tunnel experimental setup in the strut configuration. Side view (left, with waterline and SIT Deployment Module, SDM, highlighted and hydrophone visible on the left) and front view (right, without SDM)

coefficient C_P defined as follows:

$$C_P = \frac{P}{\frac{1}{2}\rho U_\infty^3 A}, \qquad C_T = \frac{T}{\frac{1}{2}\rho U_\infty^2 A},$$

$$C_Q = \frac{Q}{\frac{1}{2}\rho U_\infty^2 AR}, \tag{1}$$

where ρ, $A = \pi R^2$, and $P = Q\omega$ are, respectively, the fluid density at $20\,°C$, the rotor swept area, and the power.

A separate round of measurements was carried out at the same flow speed and λ conditions with a blade-less dummy hub replacing the rotor according to the ITTC recommended procedure 7.5-02-03−02.1, propeller open water test (ITTC-Propulsion-Committee 2021b). Measured thrust and torque were used to correct the measurements obtained with the rotor by subtracting the hub contribution and assuming a linear behavior of the rotor-hub system.

In the following, turbine performance coefficients are presented with hub correction and by normalizing values with respect to the corresponding maximum values in the no-strut condition, by comparing all tested flow speed cases:

$$\hat{C}_T = \frac{C_T}{C_{Tmax}}; \quad \hat{C}_Q = \frac{C_Q}{C_{Qmax}}; \quad \hat{C}_P = \frac{C_P}{C_{Pmax}}. \tag{2}$$

The $D = .5$ m-diameter turbine yields a 2.4% blockage, determined as the ratio between the rotor swept area and the facility cross-section area. Recalling the analysis carried out in Gaurier et al. (2015), this corresponds to a power coefficient about 3% higher than the actual value under design TSR conditions ($\lambda = 5$).

Cavitation tests were carried out by dropping the pressure in the test chamber to simulate a range of conditions at full scale. The oxygen content in the water achieves a stable condition of equilibrium with the facility static pressure in less than 2–3 min, depending on the velocity and on the static pressure in the facility. To monitor the water quality during the transient phases (change of inflow velocity and pressure) and to verify that a stable water quality condition is achieved, a dissolved oxygen meter is used. Similitude of cavitating-flow conditions between full scale and model scale can be controlled through the so-called cavitation number. In the present study, the following expression of the cavitation number has been used:

$$\sigma_{0.7} = \frac{Ps_{0.7} - P_v}{\frac{1}{2}\rho U_{0.7}^2}, \tag{3}$$

where P_v is the vapor pressure at testing conditions, and $Ps_{0.7}$ is the static pressure at the $0.7R$ blade section when positioned at full upright position, whereas $U_{0.7} =$
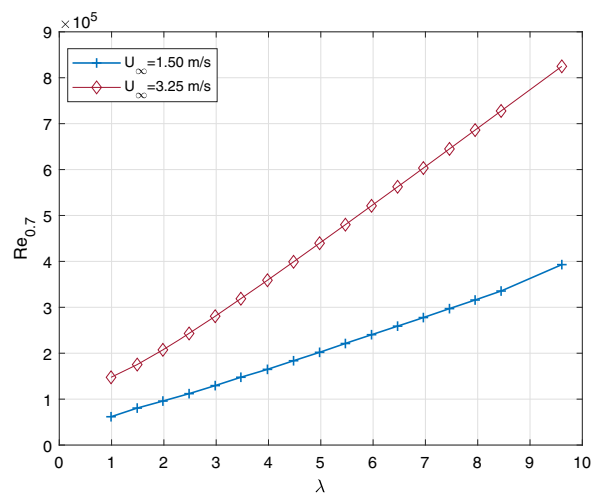

Fig. 5 Reynolds number range versus tip-speed ratio λ. Lower and upper limits based on inflow speed $U_\infty = 1.5\,m/s$ and $U_\infty = 3.25\,m/s$ respectively

$\sqrt{U_\infty^2 + (0.7\omega R)^2}$ is the total velocity at 70% of blade span. The resulting Reynolds number is calculated as follows:

$$Re_{0.7} = \frac{\rho U_{0.7} c_{0.7}}{\mu}, \tag{4}$$

where $c_{0.7}$ represents the rotor blade chord 70% of blade span and μ is the water kinematic viscosity at the test temperature, i.e., 21 C°. In Fig. 5, the variability of the Reynolds number over the considered TSR range at the lowest and highest inflow speed, respectively, $U_\infty = 1.5\,m/s$ and $U_\infty = 3.25\,m/s$, is illustrated. It can be noted that only few tested conditions are characterized by $Re_{0.7} < 2 \cdot 10^5$, whereas at the highest flow speed and λ, $Re_{0.7} \simeq 8 \cdot 10^5$ is obtained. In such conditions, it is assumed that the extension of laminar flow on the blades is limited to the blade leading edge and provides a small contribution to turbine loads.

For all testing conditions, the turbine depth was kept constant, with rotor shaft at 1.5 D below the free surface. Such an immersion was chosen after a preliminary round of tests to ensure that turbine performance measurements are negligibly affected by free-surface effects, including the wash generated by the model SDM structure.

3 Results

3.1 Cavitation analysis

The analysis of different cavitating-flow phenomenologies and the impact on turbine performance is carried out by varying the pressure inside the test channel, the inflow speed U_∞, and the turbine rotational speed ω. This results into a combi-

nation of onset flow and turbine loading conditions, so that a cavitation bucket in the (λ, σ_{07}) plane can be determined.

The different phenomenologies are described here for some representative cases selected from the full test matrix. Specifically, Fig. 6 refers to cases $\lambda = 6.5$, $U_\infty = 3\,m/s$, and behind–strut configuration, whereas Fig. 7 describes cases $\lambda = 7.5$ and $U_\infty = 2\,m/s$ for the no-strut configuration. The images show the blade-suction side observed by the two cameras, which are arranged as set out in the previous sections. The turbine is rotating clockwise as seen from upstream. The gap between the rotor boss and the model SDM upstream is visible in Fig. 6 and amounts to 5 mm. Starting from ambient conditions, pressure was gradually reduced and flow visualizations as well as operational parameters were recorded to characterize the different cavitation regimes. Once the lowest pressure (approximately 130 mbar) was reached, tests were repeated by increasing the channel pressure back to confirm the repeatability of the process. As pressure is gradually reduced from ambient conditions, the earliest appearance of water vaporization into cavity bubbles denotes the *cavitation inception* condition. Common to all types of lifting surfaces, this phenomenon occurs in the tip-vortex region (tip-vortex cavitation). This condition is illustrated in the top Fig. 6.
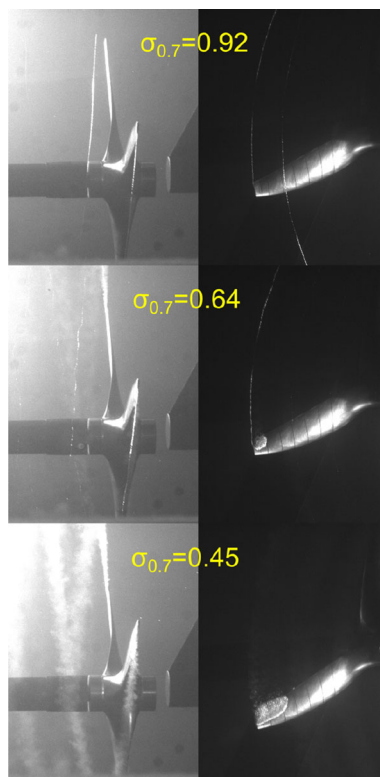

Fig. 6 Cavitation patterns on turbine blades at flow speed $U_\infty = 3\,m/s$, $\lambda = 6.5$ and varying cavitation numbers, behind-strut configuration. Visualization of tip-vortex cavitation (top), mid-chord cavitation onset (center), and fully developed mid-chord cavitation (bottom) as seen from the front camera (left) and the tilted camera (right)
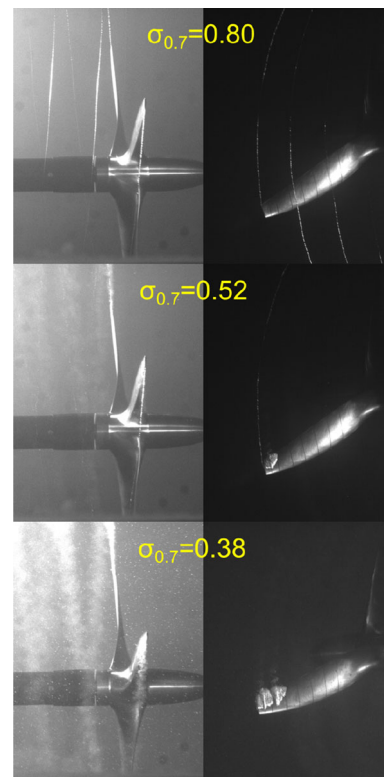

Fig. 7 Cavitation patterns on turbine blades at flow speed $U_\infty = 2\,m/s$, $\lambda = 7.5$ and varying cavitation numbers, no-strut configuration. Visualization of tip-vortex cavitation (top), mid-chord cavitation onset (center), and fully developed mid-chord cavitation (bottom) as seen from the front camera (left) and the tilted camera (right)

Tip-vortex cavitation is reported to be initially intermittent, whereas it becomes more stable at lower cavitation numbers, as shown in top Fig. 7. As pressure is further reduced, a different cavitation pattern emerges on the rotor blade suction side (center figure). A small vaporized-flow region attached to the blade surface (sheet cavity) forms at radial sections close to the tip. The front of the sheet cavity is located downstream of the blade leading edge. At blade tip, the sheet cavity detaches and is shed into the tip vortex. Inspection of the front camera (left side of figures) reveals that under these conditions, the vaporized flow in the tip vortex tends to be unstable and loses coherency as soon as it detaches from the blade tip. The cavity breaks into a cloud of microbubbles that are shed by the rotor wake as observed in left Fig. 6 and Fig. 7.

As pressure is further decreased, mid-chord cavitation patches tend to cover larger portions of the blade-suction side by expanding to inner radial sections, as seen in bottom Figs. 6 and 7. Observation of images suggests that a large cavitation patch is formed by merge of multiple cavities which stem from bubbles bursts. We point out that inspection of Fig. 6 shows the onset of cloud cavitation stemming from the mid-chord patch, which is noticeable in particular from the frontal view (on the left). Interestingly, tip-vortex cavita-

tion no longer coexists at this stage. A possible of explanation lies into the blade loading reduction as shown later on in this section.

During cavitation tests, turbine thrust and torque were recorded to correlate cavitation patterns and blade loading conditions, and to analyze the effect of cavitation on the power generated by the turbine. Cavitation bucket diagrams were thus generated by identifying (λ, σ_{07}) pairs for which the formation of bubbles in the tip-vortex region was observed. For the purpose of inception classification, intermittent tip-vortex cavitation was not considered, whereas only fully developed tip-vortex cavitation was considered. Next, cavitating-flow performance diagrams were generated by matching the observed cavitation patterns to the turbine power coefficient C_P. Results are shown in Figs. 8 and 9 for inflow speed conditions $U_\infty = 2$ and $3 \, m/s$, respectively. For both cases, results for the isolated turbine case (no–strut condition) are presented on the right side, whereas the behind–strut condition is presented on the left side. The red dots denote (λ, σ_{07}) pairs of all tested conditions. Power coefficient values are normalized with respect to the maximum value as indicated in Eq. (2).

Considering the no–strut configuration at flow speed $U_\infty = 2 \, m/s$ (right Fig. 8), ambient pressure conditions approximately correspond to $\sigma_{07} = 4$ at $\lambda = 5$. Recalling the definition of the cavitation number σ_{07} in Eq. (3), as the

tip-speed ratio increases, the σ_{07} number decreases. Considering all λ cases, a curve in the (λ, σ_{07}) plane can be drawn to identify ambient pressure conditions. As this condition is independent from the model configuration, the ambient pressure curve falls in the same position in left Fig. 8 for the behind-strut case.

For a given λ condition, a significant pressure (that is, σ_{07}) reduction is necessary to determine cavitation inception conditions. As observed from cavity pattern visualizations, further reduction of pressure determines the formation of mid-chord sheet cavitation. By marking the highest pressure at which cavitation inception and sheet cavitation are observed at each λ, the corresponding fronts in the (λ, σ_{07}) plane can be drawn. By comparing left and right maps, it can be noted that inception and sheet cavitation fronts are in the same positions for both no-strut and behind-strut configurations, except for the sheet cavitation front that occurs at slightly at lower σ_{07} in the high λ range for the behind-strut case.

The effect of cavitation on turbine performance can be analyzed from the power coefficient colormaps in the (λ, σ_{07}) plane. Consider first the no-strut configuration, right Fig. 8. In the cavitation-free regime, the region with C_p/C_{pmax} values close to 1 extends from $\lambda = 4.5$ to approximately 6.5. Tip-vortex cavitation has no effect on power, whereas a strong reduction is observed as fully developed sheet cavities

Fig. 8 Cavitation bucket and performance diagrams with colormaps of normalized power coefficient $\widehat{C}_p$ at $U_\infty = 2 \, m/s$. No-strut (right) and behind-strut (left) configurations. Red dots correspond to measured points
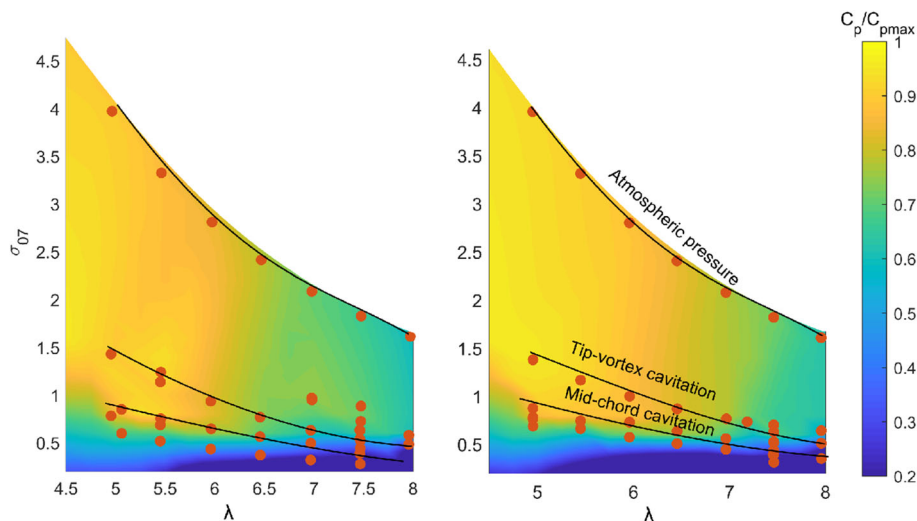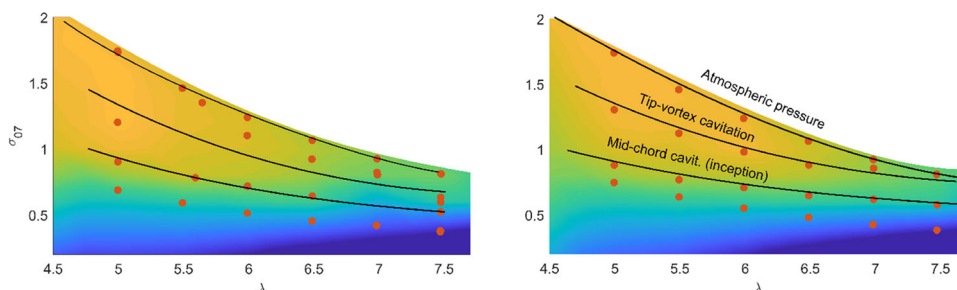

Fig. 9 Cavitation bucket and performance diagrams with colormaps of power coefficient $\widehat{C}_p$ at $U_\infty = 3 \, m/s$. No-strut (right) and behind-strut (left) configurations. Red dots correspond to measured points

form on the blade surface. At the lowest pressure conditions, below $\sigma_{07} = 0.5$, the power generated by the turbine drops significantly with respect to cavitation-free conditions. In particular, the reduction is 28% and 55% at $\lambda = 5$ and $\lambda = 6.5$, respectively.

Comparing results for the no-strut configuration with those for the behind-strut case (right and left Fig. 8, respectively), it has been already noted that the fronts corresponding to different cavitation patterns look very similar. However, the power coefficient colormaps show some interesting differences. In particular, in the λ region between 6.5 and 7, the behind-strut configuration reveals a slightly lower power than the isolated turbine case. This aspect will be analyzed in more details in the next section.

A similar analysis can be done by considering results at onset flow speed $U_\infty = 3\,m/s$, in Fig. 9, with no-strut condition (right) and behind-strut condition (left). As expected from the definition, Eq. (3), increasing onset flow speed from 2 to 3 m/s, the cavitation number corresponding to ambient pressure conditions is significantly lower, with, as an example, $\sigma_{07} = 1.75$ at $\lambda = 5$. Under $U_\infty = 3\,m/s$ conditions, a small reduction of pressure is sufficient to achieve cavitation inception. In fact, ambient pressure and cavitation inception fronts are very close and their distance reduces as λ increases. In particular, at $\lambda = 7.5$, no-strut case, cavitation inception occurs at ambient pressure as pointed out by the overlapping of the atmospheric pressure and tip-vortex cavitation front lines. A general trend is also noted that both cavitation inception and sheet cavitation fronts at $U_\infty = 3\,m/s$ fall at slightly lower σ_{07} values than in the $U_\infty = 2\,m/s$ case depicted in Fig. 8.

3.2 Performance analysis

The analysis of flow visualizations and cavitation bucket and performance diagrams discussed in the previous section reveals that the occurrence of cavitation may have a significant impact on the hydrodynamic power generated by the turbine. Similarly, the presence of the support structure upstream of the rotor is also responsible for a small reduction of turbine performance, whereas a marginal impact on cavitation was observed.

In the present section, quantitative comparisons of turbine power, torque, and thrust for all the tested conditions for with and without strut configurations are presented and discussed.

The mean values of C_P, C_Q, and C_T coefficients measured at ambient pressure and different onset flow speed U_∞ are shown in Fig. 10 for the no-strut condition, and in Fig. 11 for the behind-strut condition. Plotted coefficients are normalized as described in Eq. 2. Uncertainty of mean values is below 1% with a 95% confidence interval based on a t-Student distribution. Error bars are within symbol size.
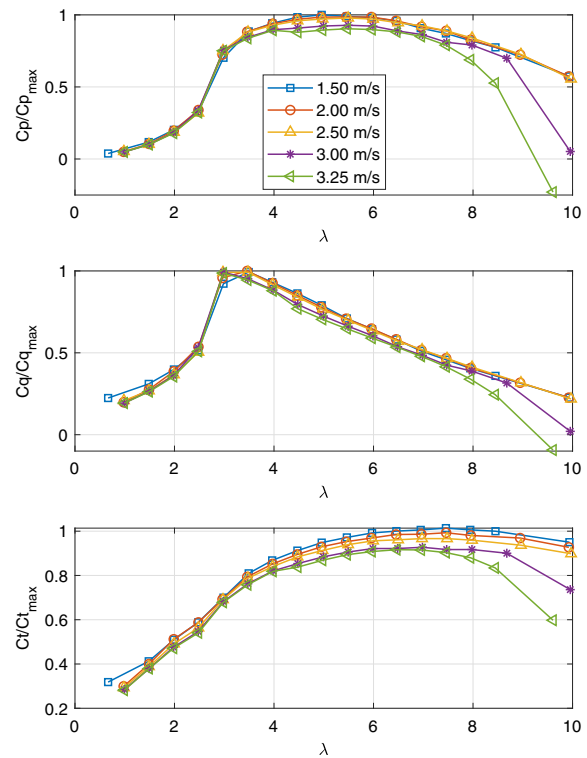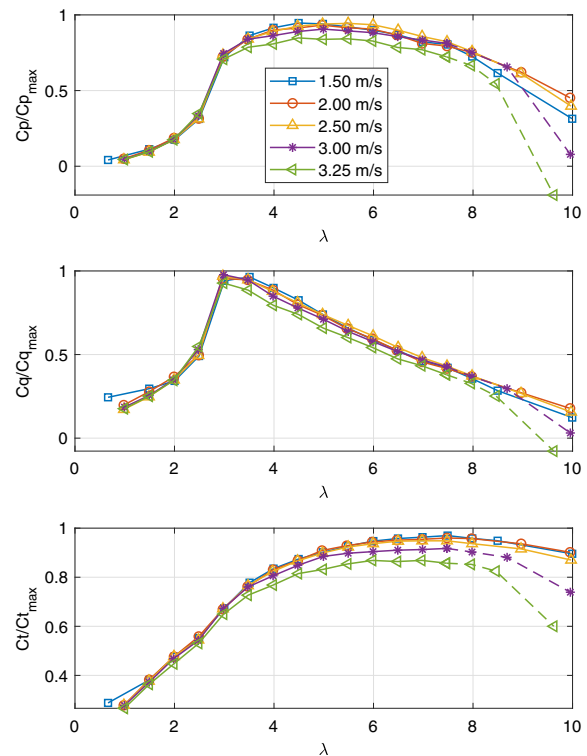

Fig. 10 Turbine normalized performance coefficients $\widehat{C_P}$ (top), $\widehat{C_Q}$ (center), and $\widehat{C_T}$ (bottom) versus tip speed ratio λ. All inflow speed cases, no-strut configuration

Fig. 11 Turbine normalized performance coefficients $\widehat{C_P}$ (top), $\widehat{C_Q}$ (center), and $\widehat{C_T}$ (bottom) versus tip-speed ratio λ. Dotted lines indicate cavitating conditions. All inflow speed cases, behind-strut configuration

Analysis of the power coefficient C_P in the no-strut configuration (top Fig. 10) shows that the model turbine yields more than 90% of peak power over a quite large λ range, approximately between 4 and 7. Performance deterioration due to stall occurs as the λ is reduced below 3. The stall condition can be clearly identified from the torque curve (center Fig. 10). Throughout the tested λ range, torque and power data for onset flow speed between 1.5 and 2.5 m/s are identical within plotting accuracy. Lower values for both C_P and C_Q are found at the highest tested flow speed, $U_\infty = 3.25\,m/s$. In particular, results for these two cases denote significantly lower values in the high λ range, approximately above λ = 8.5 for the $U_\infty = 3\,m/s$ case, and λ = 8 for the $U_\infty = 3.25\,m/s$ case. Recalling the cavitation bucket and performance diagrams discussed in the previous sections, Figs. 8 and 9, the observed torque and power reduction is the effect of the formation of cavities on the blade surface. As already noticed, at the highest tested flow speeds and λ, cavitation on the model turbine blades occurred also at ambient pressure.

A similar trend is observed from thrust coefficient measurements, bottom Fig. 10. The occurrence of cavitation at high onset flow speed and λ determines a strong reduction of the blade loading. A closer look at results for $U_\infty = 3\,m/s$ reveals the increase of all performance coefficients in a narrow λ range at 8 ≤ λ ≤ 8.7. This behavior can be explained with the formation of attached sheet cavities on portions of the blade-suction side as shown in the previous section. The noted effect on blade loads is well known on marine propellers (Pereira et al. 2004). A stable sheet cavity determines a virtual increase of blade section camber with a consequent increase of sectional lift force. As flow conditions determine a further growth and destabilization of the cavity, this effect vanishes and a drop of sectional lift occurs.

The results for the behind–strut configuration in Fig. 11 show trends very similar to those described for the no-strut condition. The normalization of performance coefficients according to Eq. (2) allows to have a direct comparison between the two configurations. The presence of the strut upstream of the rotor determines a modest reduction of turbine thrust, torque, and power with respect to the isolated turbine case. As an example, the peak power measured at $U_\infty = 2.5\,m/s$ is 5% lower of the corresponding peak value of the no-strut configuration.

The comparison of measured thrust and torque at different flow speed U_∞ for both no-strut and behind-strut configurations reveals an unexpected trend. Common experience from theory and past experimental studies is that torque (and hence power) increases with onset flow speed as an effect of reducing viscous friction on blades at higher Reynolds numbers. An opposite effect is observed on thrust, that reduces as the flow speed increases, as shown in Sarichloo et al. (2018), with experimental and computational results

on an SIT 250 turbine similar to the present case. Results in Figs. 10 and 11 show a different phenomenology, with the above-mentioned Reynolds number effect canceled for flow speeds between 1.5 and 2.5 m/s and even an opposite trend at $U_\infty = 3$ and $3.25\,m/s$, with both torque and thrust reducing as the flow speed increases. A possible explanation could be found in blade twisting under higher hydrodynamic loads as flow speed increases. Induced twist results into lower angle of attack of blade sections and hence reduced thrust and torque. This phenomenology has been observed in past model scale tests of similar SIT blade design (Kaufmann et al. 2019). The stacking line of the SIT250 blades is designed to provide a sufficiently high torsional moment to support passive-adaptive pitch control. Thus, a *passive pitch* behavior is possible even for an isotropic material like stainless steel used for the manufacturing of small-scale model turbines. Further analysis on this point is required to confirm the present hypothesis.

Additional insight into turbine performance is given by the Root Mean Square (RMS) of thrust and torque over the λ range which are presented in Fig. 12 (no-strut condition) and Fig. 13 (behind-strut condition). These distributions are helpful to analyze the occurrence of blade loading fluctuations under varying operating conditions.

RMS values of a generic quantity F are calculated according to the following expression:

$$RMS(F) = \sqrt{\frac{1}{N} \sum_{i=1}^{N} \left(F_i - \overline{F}\right)^2}, \tag{5}$$

where the overbar indicates the mean value of the quantity and N is the number of data samples.

As expected, thrust and torque fluctuations have the highest values in the turbine stall regime that, as shown above,
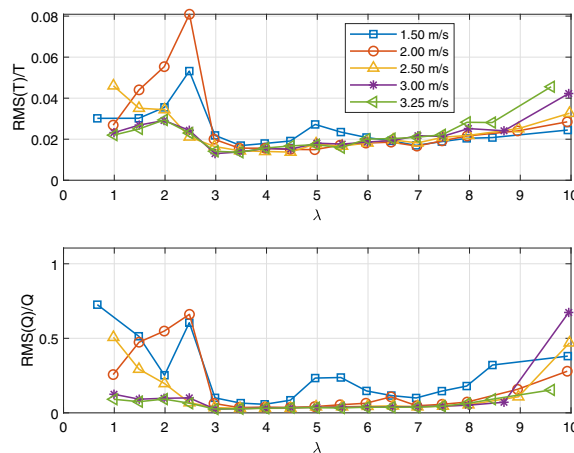

Fig. 12 Root mean square of turbine thrust T (top) and torque Q (bottom) versus tip-speed ratio λ. Values normalized against average quantities. All inflow speed cases, no-strut configuration
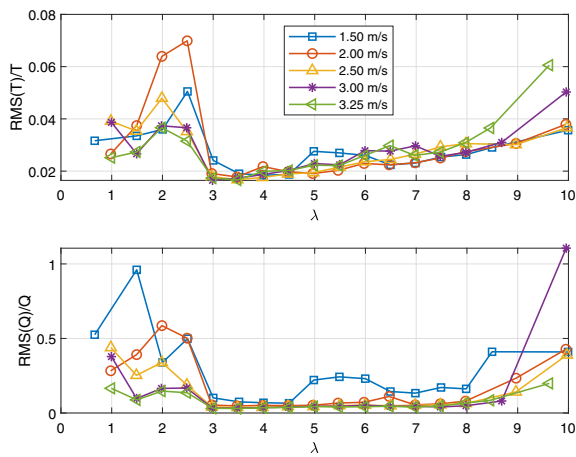
Fig. 13 Root mean square of turbine thrust T (top) and torque Q (bottom) versus tip-speed ratio λ. Values normalized against average quantities. All inflow speed cases, behind-strut configuration

occurs for $\lambda < 3$. For higher λ conditions, load fluctuations are very small except in the highest tested λ cases. This phenomenology is associated with the presence of cavitation on the blades. In particular, it can be noted that the RMS values are large in the same high λ range where a significant reduction of thrust and torque mean values due to cavitation effects have been observed; see Fig. 10 for the no–strut condition, and Fig. 11 for the behind–strut condition. Comparing results at different onset flow speed, as expected, the fluctuations at high λ associated with cavitation on blades are larger as the flow speed increases. A peculiar behavior with respect to the general trends is noted only for the lowest flow speed case, $U_\infty = 1.5\,m/s$, with higher RMS values of torque as compared to results at higher flow speed. This result can be interpreted as an effect of the instability of the transition between laminar and turbulent boundary layer on the blades in the low Reynolds number condition at the lowest tested flow speed, $U_\infty = 1.5\,m/s$ for which $Re_{0.7} \approx 200000$ at $\lambda = 5$. The effect on torque is apparent, whereas it is limited to a narrow λ range for the thrust case. Finally, the comparison between the configuration without and with the supporting structure (Fig. 12 and Fig. 13, respectively) shows, as expected, as small increase of RMS (load fluctuations) in conditions where the strut wake perturbs the inflow to the turbine blades.

3.3 Radiated noise

In addition to flow visualizations and blade loading measurements, the analysis of acoustic noise signatures provides further insight to the effects of cavitation on tidal turbines. In the present study, acoustic signals were acquired by an hydrophone placed at a distance of one turbine diameter from the rotor axis and located perpendicular to the plane of the rotor, as shown in Fig. 4.

Results of raw signals processing are presented in Fig. 14 as power spectrum density (PSD) of the measured acoustic pressure. Each acquisition covers a time window of 25 s to reduce the impact of any instantaneous noise source. The PSD is estimated via the Welch method with a Hamming window function. The 95% confidence interval of the measurement lies within the line thickness of the plots. Configurations without and with strut are given in top and bottom diagrams, respectively. Recalling cavitation maps in Figs. 8 and 9, conditions at ambient pressure (cavitation free), $\sigma_{07} = 1.35$ (tip-vortex cavitation), and $\sigma_{07} = 0.7$ (fully developed sheet cavitation) at onset flow speed $U_\infty = 3\,m/s$ and $\lambda = 5$ are compared. Acoustic pressure PSD is presented as dB over a frequency range between 0 and 25000 Hz. Recalling the model turbine is three-bladed, the above flow and operating conditions correspond to a blade passing frequency of 28.66 Hz. Comparing the different pressure conditions in Fig. 14, it is apparent that the occurrence of vaporized-flow regions determines a significant increase of the emitted noise. In the low-frequency range, below 8000 Hz, the increase of noise levels due to tip-vortex cavitation is quite limited in the no-strut configuration (top Fig. 14, and relatively larger in the behind-strut case (bottom figure). Larger effects are noted at higher frequency (broadband noise), as a consequence of the collapse of microbubbles in the tip vortex. Results for the tip-vortex cavitation condition are in agreement with the findings on a similar study in Shi et al. (2016). When pressure
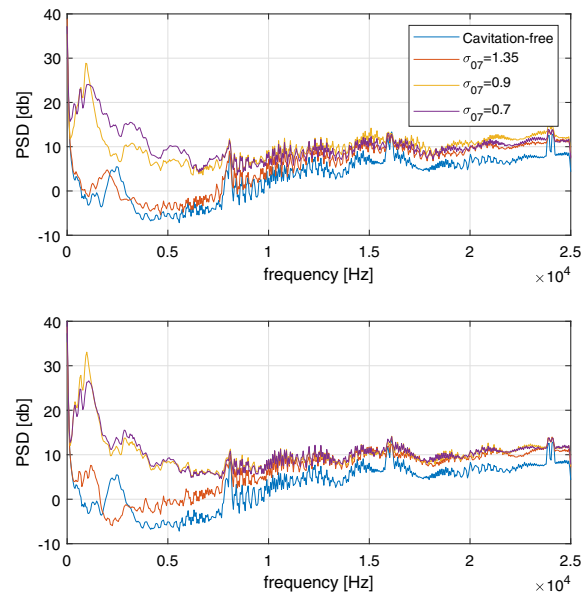

Fig. 14 Power spectrum density of acoustic noise signatures. Cavitation-free and cavitating-flow conditions compared for case $U_\infty = 3\,m/s$ and $\lambda = 5$. No-strut (top) and behind-strut (bottom) configurations. Confidence interval of 95% lies within the plot lines' thickness

is further reduced and cavities appear on the blade surface, an increase of noise levels up to 20 dB is observed in the low-frequency band 500–7000 Hz. In the higher frequency range, noise levels are comparable to those observed under tip-vortex cavitation conditions.

3.4 Effect of the support structure on turbine performance and cavitation

The impact of the perturbation induced by the support structure on turbine performance can be further analyzed by considering power curves in Fig. 15 and thrust curves in Fig. 16, where two different onset flow speeds, $U_\infty = 2, 3 \, m/s$, are considered. In this case, normalized dimensional power and thrust are presented, to highlight differences between measurements at variable onset flow speed. Measured quantities are divided by the maximum power and thrust measured over the experimental campaign, i.e., P_{max} and T_{max}, obtained at the maximum inflow speed tested. Both thrust and power curves show that the support structure has no effect on the turbine stall regime that occurs at $\lambda < 3$, whereas it determines a reduced power at higher λ; see Fig. 15. In the same operating range, turbine thrust is only marginally affected by the presence of the strut; see Fig. 16. These results can be explained by considering the flow perturbation induced by the wake shed by the upstream strut. Turbulent structures in the strut wake stimulate the destabilization of the flow on the turbine blade surface, and the formation of larger portions of turbulent boundary layer. This corresponds to an increase of friction with respect to the uniform onset flow case (no-strut configuration). The negative torque is responsible for the reduction of generated torque and power, whereas the effect on thrust is negligible. Lack of significant differences between thrust measurements in the configurations with and without strut also highlights that the expected reduction of the mass flow rate across the rotor
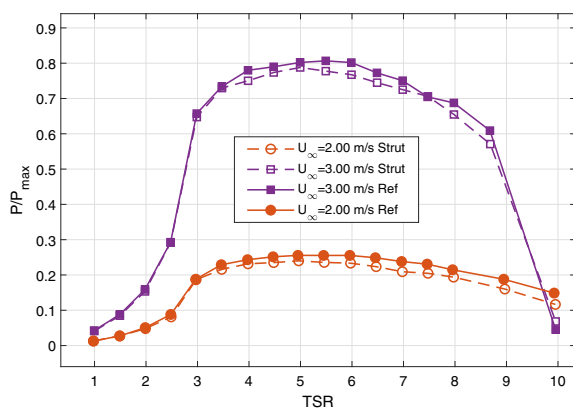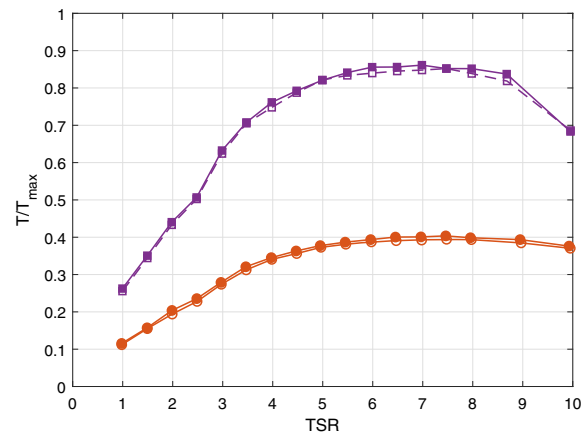

Fig. 16 Normalized dimensional thrust for two inflow speed cases: $U_\infty = 2$ and $3 \, m/s$. Configurations with and without supporting structure compared

disc due to the strut wake is limited. In fact, the behind-strut configuration determines a 2.6% blockage, based on the dimensions in Fig. 3, which is only 8% higher than the no-strut configuration.

The very limited effect of the upstream strut on the loadings on turbine blades also explains the very similar cavitation patterns in both no-strut and behind-strut configurations. Combining the analysis of results on both turbine performance, cavitation risk, and radiated noise, the following conclusions regarding the presence of the supporting structure upstream of the turbine can be drawn:

- the turbine in behind-strut conditions at model scale generates about 10% less peak power than the turbine in uniform onset flow. This effect has been explained with additional passive torque that is generated by the turbulent structures shed by strut wake and interacting with the blade boundary layer. At full scale, it is expected that this phenomenon tends to be negligible due to the tidal flow turbulence. This phenomenology has a limited impact on turbine thrust (Figs. 10 and 11)
- cavitation inception is marginally affected by the presence of the strut. The same trend is observed for the development of cavities attached on the surface of the blades (Figs. 6 and 7)
- the wake shed by the strut determines a moderate increase of the acoustic noise that is generated by tip-vortex cavitation (Fig. 14)

It is worth to observe that the above conclusions are valid for the present turbine/support structure layout and testing conditions. In particular, the overall limited nuisance induced by the strut on turbine performance is due to the design of the strut, characterized by sections having a small thickness and creating a very limited blockage in front of the rotor. Another

Fig. 15 Normalized dimensional power for two inflow speed cases: $U_\infty = 2$ and $3 \, m/s$. Configurations with and without supporting structure compared

important aspect to consider is that the results discussed here reflect small-scale testing conditions characterized by relatively low Reynolds number regimes as compared to the full-scale case. It is expected that some of the above-mentioned effects are further reduced in the operation of a full-scale turbine, where Reynolds number is approximately ten times higher and the onset flow turbulence in the tidal stream filters the effect of small eddies in the strut wake.

It may be concluded that an accurate design of an upstream support structure can help the developer to achieve an adequate compromise between a limited reduction of power output and the potential benefits that can result from easier access for maintenance.

4 Conclusions

The perturbation induced by an upstream support structure on the performance and cavitation of a horizontal-axis turbine has been investigated by an experimental campaign at model scale. The turbine and support structure reproduce the installation of Schottel Hydro SIT Turbines on the Plat-I floating barge. Model tests have been performed in a depressurized water flume facility under variable inflow speed and pressure conditions. Flow visualizations by high-speed cameras and radiated noise recordings synchronized with turbine thrust and torque measurements provided an extensive dataset on turbine operation in both idealized (no-strut) and real (behind-strut) conditions. Model tests allowed to estimate cavitation-induced performance losses in tidal turbines operating at relatively small depth, as in the case of floating devices. The combined analysis of flow visualizations and performance measurements showed that:

- tip-vortex cavitation does not affect turbine performance, whereas a limited increase of noise emissions is observed.
- a marked decrease of turbine performance is associated with the formation of sheet cavities attached to the blade-suction side and higher radiated noise levels. Flume tank data extrapolation to full scale reveals that this phenomenology can be present on turbines in the overspeed condition at high λ.
- the presence of a support structure upstream of the turbine only leads to a limited reduction of power, whereas the thrust is not affected. This effect is expected to be smaller in real sea conditions, as the onset flow is already highly turbulent.
- the upstream perturbation was reported to delay the progression of sheet cavitation along the rotor blade surface in a way which is independent from the inflow speed.

The data obtained from the described experimental study can be used to build a connection between turbine operating points and the likelihood of occurrence of different cavitation types at full scale in the real operating conditions. The developed experimental database provides new knowledge to improve the design of tidal turbine rotor blades.

Data availability statement Data are available upon reasonable request.

Code Availability Not applicable.

Declarations

Conflict of interest The authors have no competing interests, or other interests that might be perceived to influence the results and/or discussion reported in this paper.

Consent for publication Not applicable.

Consent to participate Not applicable.

Ethics approval Not applicable.

References

Aktas B, Atlar M, Turkmen S, Korkut E, Fitzsimmons P (2016) Systematic cavitation tunnel tests of a propeller in uniform and inclined flow conditions as part of a round robin test campaign. Ocean Eng 120:136–151

Aktas B, Atlar M, Turkmen S, Shi W, Sampson R, Korkut E, Fitzsimmons P (2016) Propeller cavitation noise investigations of a research vessel using medium size cavitation tunnel tests and full-scale trials. Ocean Eng 120:122–135

Bahaj A, Myers L (2004) Analytical estimates of the energy yield potential from the alderney race (channel islands) using marine current energy converters. Renew Energy 29(12):1931–1945

Bahaj A, Molland A, Chaplin J, Batten W (2007) Power and thrust measurements of marine current turbines under various hydrodynamic

flow conditions in a cavitation tunnel and a towing tank. Renew Energy 32(3):407–426

Day A, Babarit A, Fontaine A, He YP, Kraskowski M, Murai M, Penesis I, Salvatore F, Shin HK (2015) Hydrodynamic modelling of marine renewable energy devices: a state of the art review. Ocean Eng 108:46–69

Frisk GV (2012) Noiseonomics: The relationship between ambient noise levels in the sea and global economic trends. Sci Rep 2(1):1–4

Gajardo D, Escauriaza C, Ingram DM (2019) Capturing the development and interactions of wakes in tidal turbine arrays using a coupled bem-des model. Ocean Eng 181:71–88

Gaurier B, Germain G, Facq J, Johnstone C, Grant A, Day A, Nixon E, Di Felice F, Costanzo M (2015) Tidal energy round robin tests comparisons between towing tank and circulating tank results. Int J Marine Energy 12:87–109

Hansen A, Butterfield C (1993) Aerodynamics of horizontal-axis wind turbines. Ann Rev Fluid Mech 25(1):115–149

Hildebrand JA (2009) Anthropogenic and natural sources of ambient noise in the ocean. Mar Ecol Progress Ser 395:5–20

ITTC-Propulsion-Committee (2017) Model scale cavitation test. Recommended procedure 7.5-02-03-03, International Towing Tank Conference (ITTC)

ITTC-Propulsion-Committee (2021a) Model tests for current turbines. Recommended procedure 7.5-02-07-03.9, International Towing Tank Conference (ITTC)

ITTC-Propulsion-Committee (2021b) Open water test. Recommended procedure 7.5-02-03-02.1, International Towing Tank Conference (ITTC)

Jeffcoate, (2021) Comparisons between flood and ebb performance of plat-i in nova scotia. Proc Euro Wave Tidal Energy Conf 87:240–252

Jeffcoate P, Starzmann R, Elsaesser B, Scholl S, Bischoff S (2015) Field measurements of a full scale tidal turbine. Int J Mar Energy 12:3–20

Kaufmann N, Carolus T, Starzmann R (2017) An enhanced and validated performance and cavitation prediction model for horizontal axis tidal turbines. Int J Mar Energy 19:145–163

Kaufmann N, Carolus T, Starzmann R (2019) On the effect of elastic blade deformation on the performance of a horizontal axis tidal current turbine. In: Thirteen European Wave and Tidal Energy Conference, Naples, Italy

Kempener R, Neumann F (2014) Tidal energy technology brief. International Renewable Energy Agency (IRENA) pp 1–34

Lee J, Kim Y, Khosronejad A, Kang S (2020) Experimental study of the wake characteristics of an axial flow hydrokinetic turbine at different tip speed ratios. Ocean Eng 196(106):777

Mycek P, Gaurier B, Germain G, Pinon G, Rivoalen E (2014) Experimental study of the turbulence intensity effects on marine current turbines behaviour. part i: one single turbine. Renew Energy 66:729–746

Mycek P, Gaurier B, Germain G, Pinon G, Rivoalen E (2014) Experimental study of the turbulence intensity effects on marine current turbines behaviour. part ii: Two interacting turbines. Renew Energy 68:876–892

Pereira F, Salvatore F, Di Felice F (2004) Measurement and modelling of propeller cavitation in uniform inflow. J Fluids Eng 126:671–679

Rosli R, Shi W, Aktas B, Norman R, Atlar M (2020) Cavitation observations, underwater radiated noise measurements and full-scale predictions of the hydro-spinna turbine. Ocean Eng 210(107):536

Sarichloo Z, Salvatore F, Di Felice F, Costanzo M, Starzmann R, Frost C (2018) Computational analysis and experimental verification of a boundary integral equation model for tidal turbines. In: Third International Conference on Renewable Energies Offshore, RENEW 2018, Lisbon, Portugal

Shi W, Atlar M, Rosli R, Aktas B, Norman R (2016) Cavitation observations and noise measurements of horizontal axis tidal turbines with biomimetic blade leading-edge designs. Ocean Eng 121:143–155

Starzmann, (2021) Effect of fouling on the performance of an instream turbinecomparisons between flood and ebb performance of plat-i in nova scotia. Proceedings of the European Wave and Tidal Energy Conference 87:240–252

Sun Z, Li D, Mao Y, Feng L, Zhang Y, Liu C (2022) Anti-cavitation optimal design and experimental research on tidal turbines based on improved inverse bem. Energy 239(122):263

Wang D, Atlar M, Sampson R (2007) An experimental investigation on cavitation, noise, and slipstream characteristics of ocean stream turbines. Proc Inst Mech Eng Part A 221(2):219–231

Wimshurst A, Vogel C, Willden R (2018) Cavitation limits on tidal turbine performance. Ocean Eng 152:223–233